# Optimal interactions of light with magnetic and electric resonant particles

Rémi Colom,[1,2] Alexis Devilez,[1] Nicolas Bonod,[1] and Brian Stout[1,*]

[1]*Aix-Marseille Université, CNRS, Centrale Marseille, Institut Fresnel, UMR 7249, Campus de Saint Jérôme, 13397 Marseille, France*

[2]*Centre for Ultrahigh-Bandwidth Devices for Optical Systems (CUDOS), University of Sydney, Sydney, NSW 2006, Australia*

(Received 8 October 2015; revised manuscript received 17 December 2015; published 27 January 2016)

This work studies the limits of far- and near-field electromagnetic responses of subwavelength scatterers, like the unitary limit of lossless scatterers and the ideal absorption limit of lossy particles. These limit behaviors are described in terms of analytic formulas that approximate finite-size effects while rigorously including radiative corrections. This analysis predicts the electric and/or magnetic limit responses of both metallic and dielectric nanoparticles while quantitatively describing near-field enhancements.

DOI: 10.1103/PhysRevB.93.045427

## I. INTRODUCTION

Photonic resonances in subwavelength dielectric or metallic scatterers have generated keen interest on account of their ability to induce strong light-matter interactions near subwavelength particles [1–4]. Optimizing the resonant interaction between light and such particles appears to be of fundamental importance to improve the efficiency of light scattering and increase near-field enhancements [5–7]. Light-particle interactions are usually quantified by calculating the absorption and scattering cross sections [8–10]. The question addressed in this work is how to reach their theoretical limits in order to maximize light scattering or absorption by metallic or dielectric photonic resonators and how to quantify the accompanying near-field enhancements.

The $T$-matrix formalism [11] has long proven quite useful in describing light scattering by particles since it provides a *complete* scattering solution in a relatively intuitive manner. However, recent literature in optics has emphasized that alternate scattering formulations, like the $S$ and $K$ matrices, provide useful complementary descriptions of light-matter interactions that shed additional light on conservation laws and limit behaviors [12,13].

In this work, we use these alternative formulations to derive approximate formulas which can describe the resonant and off-resonant responses of small spheres of any size and composition. Although the studied optical response limits also apply to particles of arbitrary shape, spherical symmetry is ideal for analytically defining the limit behaviors. More precisely, we use the Laurent expansion of the inverse $K$ matrix, and we obtain highly accurate energy-conserving approximations to the electromagnetic response of small particles.

These accurate approximations are used to define the unitary limit (UL) and ideal absorption (IA) conditions. The limits are first investigated in the case of plasmonic nanoparticles, but particular interest is then devoted to the magnetic modes hosted by dielectric particles. Magnetic modes are very promising to enhance light-matter interaction and we derive the analytic formulas of dielectric permittivities that optimize light-matter interaction via magnetic-mode excitation [14–20]. We also give formulas that can accurately predict near-field enhancements around the particles.

## II. ELECTROMAGNETIC RESPONSE OF SUBWAVELENGTH-SIZED PARTICLES

Let us consider a scatterer characterized by a permittivity $\varepsilon_s$ and permeability $\mu_s$, placed in a background medium of permittivity $\varepsilon_b$ and permeability $\mu_b$ (index $N_b = \sqrt{\varepsilon_b \mu_b}$). The scattering by a homogeneous spherically symmetric scatterer is completely characterized by its multipolar Mie coefficients, which are opposite in sign to the $T$-matrix coefficients detailed in Appendix A, $a_n = -T_n^{(e)}$ and $b_n = -T_n^{(h)}$ [where superscripts $(e)$ and $(h)$ designate electric and magnetic modes, respectively].

Although $T$ matrices contain all the scattering information, it proves convenient to transform them into other forms like $S$ matrices and reaction matrices, $K$. A brief review of the essential theory behind these transformations is given in Appendix A, but in this work we exploit the following relationship between the $T$ and the $K$ matrices (see also Ref. [13]):

$$K = iT(I+T)^{-1} \Leftrightarrow T^{-1} = iK^{-1} - I. \tag{1}$$

The relations of Eq. (1) allow the following expressions for the Mie coefficients:

$$a_n^{-1} = -i\left(K_n^{(e)}\right)^{-1} + 1, \tag{2a}$$

$$b_n^{-1} = -i\left(K_n^{(h)}\right)^{-1} + 1. \tag{2b}$$

There is a distinct advantage in writing the Mie coefficients in this manner since, as shown in Appendix A, the reaction matrix elements, $K_n = -\tan\delta_n$, must be real valued for lossless scatterers with no intrinsic loss (the *scattering phase shifts*, $\delta_n$, are also real valued for lossless scatterers as discussed in Appendix A and in Ref. [8], chap. 10. A direct consequence of Eqs. (2) is that any real-valued approximation to $K_n$ in Eq. (4) will preserve the energy conservation relations for the Mie coefficients of *lossless* scatterers (i.e., $\mathrm{Re}\{a_n\} = |a_n|^2$ and $\mathrm{Re}\{b_n\} = |b_n|^2$ for lossless scatterers).

The relations of Eq. (2) are a multipole generalization of the well-known *energy conserving* representation of the electric dipole polarizability, $\alpha_e$, where $\alpha_e$ embodies the linear relationship between the excitation field and the object's induced electric dipole moment, $\mathbf{p} = \epsilon_0 \varepsilon_b \alpha_e \mathbf{E}_{\mathrm{exc}}$. Energy conserving

*brian.stout@fresnel.fr

 

approximations to the frequency-dependent polarizability, $\alpha_e$, have long been known to take the form [12,21]

$$\alpha_e^{-1} = \alpha_{\text{n.r.}}^{-1} - i\frac{k^3}{6\pi}, \tag{3}$$

where $k = 2\pi/\lambda$ is the in-medium wave number.

The term $\alpha_{\text{n.r.}}$ in Eq. (3) is the "nonradiative" polarizability, often approximated by its electrostatic value even though finite-size corrections have repeatedly been proposed [12,13,21–24]. Recalling the relation between the dimensionless Mie coefficients and the polarizability [25], $\alpha_e = i\frac{6\pi}{k^3}a_1$, and defining the nonradiative polarizability in terms of the reaction matrix as $\alpha_{\text{n.r.}} \equiv -6\pi K_1^{(e)}/k^3$, Eq. (3) becomes synonymous with the electric dipole case of Eq. (2) up to an overall multiplicative factor.

The Laurent-series development of the inverse reaction matrix elements, $K_n$, in powers of $x = kR$ is given in Appendix B. Restricting our attention to the dipole term, $n = 1$, $\overline{\varepsilon}_s = \varepsilon_s/\varepsilon_b$, and $\overline{\mu}_s = 1$ for small scatterers yields

$$\left[K_1^{(e)}\right]^{-1} = -\frac{3(\overline{\varepsilon}_s+2)}{2(kR)^3(\overline{\varepsilon}_s-1)}\left(1 - \frac{3(kR)^2(\overline{\varepsilon}_s-2)}{5(\overline{\varepsilon}_s+2)} - \frac{3(kR)^4\left(\overline{\varepsilon}_s^2 - 24\overline{\varepsilon}_s + 16\right)}{350(\overline{\varepsilon}_s+2)}\right), \tag{4a}$$

$$\left[K_1^{(h)}\right]^{-1} = -\frac{45}{(kR)^5(\overline{\varepsilon}_s-1)}\left(1 - \frac{(kR)^2(2\overline{\varepsilon}_s-5)}{21} - \frac{(kR)^4\left(\overline{\varepsilon}_s^2 + 100\overline{\varepsilon}_s - 125\right)}{2205}\right). \tag{4b}$$

The fourth-order, $x^4$-sized corrections of Eqs. (4) will usually suffice, but the order-$x^6$-sized corrections in parentheses are given in Appendix B.

Long-wavelength approximations of the electric-mode Mie coefficients, like that found by inserting Eq. (4a) into Eq. (2a), have already been shown to accurately describe the electric response of small metallic spheres [13,26] as illustrated in Fig. 1, where we compare exact and approximate $a_1$ coefficients of a $R = 60$-nm-radius gold sphere [27].

It is much less appreciated, however, that the analogous procedure for magnetic modes of inserting Eq. (4b) into Eq. (2b) produces good approximations to magnetic dipole resonances in high-index dielectric spheres. The results displayed in Fig. 2 illustrate the accuracy of this method to describe the magnetic dipole coefficient of an $R = 80$ nm, $\varepsilon = 16$ dielectric sphere (despite the fact that the quasistatic magnetic polarizability is 0 due to the absence of permeability contrasts).

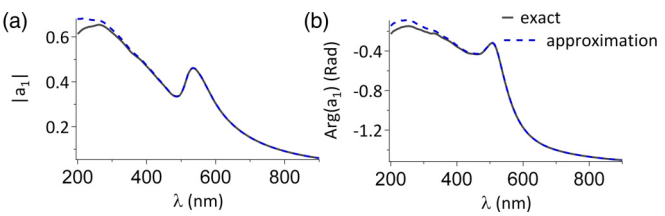


FIG. 1. Approximate values for the electric dipole Mie coefficient, $a_1$ (amplitude and phase), compared with the exact values (solid black line); $R = 60$-nm gold sphere.

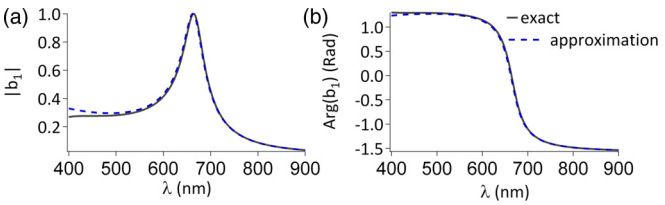


FIG. 2. Approximate values for the magnetic dipole Mie coefficient, $b_1$ (amplitude and phase), compared with the exact values (solid gray line); $R = 80$ nm, $\varepsilon = 16$.

## III. OPTIMAL LIGHT-PARTICLE INTERACTIONS

### A. Limit response conditions

The total cross sections of an arbitrary spherically symmetric scatterer are the sum of the contributions from all the multipolar modes,

$$\sigma = \sum_{n=1}^{\infty}\left\{\sigma_n^{(e)} + \sigma_n^{(h)}\right\}, \tag{5}$$

where $\sigma$ can be either the scattering, ($\sigma_{\text{s}}$), the extinction ($\sigma_{\text{e}}$), or the absorption ($\sigma_{\text{a}}$) cross section and the $n$th multipolar-mode contributions are, respectively, denoted $\sigma_{n,\text{s}}^{(q)}$, $\sigma_{n,\text{e}}^{(q)}$, and $\sigma_{n,\text{a}}^{(q)}$, with $(q) = (e)$ or $(h)$ for (electric or magnetic modes).

Expressing the modal contributions to the cross sections, $\sigma_{\text{s}}$, $\sigma_{\text{e}}$, and $\sigma_{\text{a}}$, in terms of the $S$ matrix is particularly convenient for determining optical response limits [12],

$$\begin{aligned}\sigma_{n,\text{e}}^{(q)} &= \frac{(2n+1)\lambda^2}{4\pi}\text{Re}\left\{1 - S_n^{(q)}\right\},\\ \sigma_{n,\text{s}}^{(q)} &= \frac{(2n+1)\lambda^2}{8\pi}\left|1 - S_n^{(q)}\right|^2,\\ \sigma_{n,\text{a}}^{(q)} &= \frac{(2n+1)\lambda^2}{8\pi}\left(1 - \left|S_n^{(q)}\right|^2\right),\end{aligned} \tag{6}$$

where $\lambda = \lambda_0/N_b$ is the in-medium wavelength and we recall that $|S_1^{(q)}| \leqslant 1$ for passive media ($|S_1^{(q)}| = 1$ for lossless media). The $(2n+1)$ factor in Eq. (6) results from the $2n+1$ degeneracy of the projection quantum numbers for each angular momentum number, $n$.

We henceforth adopt the usual definition for the UL as occurring whenever the contribution to the scattering cross section of at least one mode reaches its upper bound, while IA analogously occurs whenever the contribution to the absorption cross section of one mode attains its upper bound [12,28,29]. Therefore, Eqs. (6) show that the UL and IA conditions (*of a given mode at a given wavelength*) can be expressed in terms of the $S$-matrix coefficients as

$$S_{n,\text{UL}}^{(q)} = -1, \quad S_{n,\text{IA}}^{(q)} = 0. \tag{7}$$

The cross-section bounds associated with the UL and IA in an $n$th-order mode are, respectively,

$$\sigma_{n,\text{s}}^{(q)} = \sigma_{n,\text{e}}^{(q)} = \frac{(2n+1)\lambda^2}{2\pi} \quad \text{and} \quad \sigma_{n,\text{a}}^{(q)} = \sigma_{n,\text{s}}^{(q)} = \frac{(2n+1)\lambda^2}{8\pi} \tag{8}$$

The UL and IA conditions in terms of the reaction matrix coefficients $K_n$ are readily found by, respectively, inserting the conditions of Eq. (7) into Eq. (A11) Cayley transform

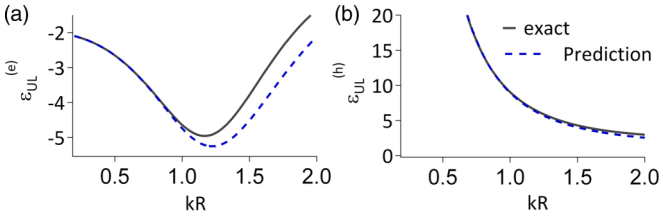


FIG. 3. Values of permittivity required to reach the dipole UL in the electric (a) and magnetic (b) modes as a function of $kR$. Exact predictions (solid gray lines) and approximate predictions [dashed (blue) lines].

relations:

$$\left[K_{n,\mathrm{UL}}^{(q)}\right]^{-1}=0,\quad \left[K_{n,\mathrm{IA}}^{(q)}\right]^{-1}=i. \tag{9}$$

In Fig. 3, we compare the exact solutions of the UL of Eq. (9) in terms of permittivity as a function of the particle size parameter, $kR$, with the algebraically obtained predictions employing the approximations of Eq. (4). One remarks that the UL permittivities are real valued as required by unitarity and inspection of Eq. (6).

Approximate predictions of IA can likewise be obtained by solving the IA condition in Eq. (9) with the approximate expression of $K_1^{(q)}$ given in Eq. (4). These are compared with exact calculations in Fig. 4. Approximate expressions are even more useful here since exact IA solutions require solving a complex transcendental equation.

One remarks that the approximate predictions for both the UL and IA in Figs. 3 and 4 are in good agreement for small size-parameters ($kR<1$) and remain close even for larger $kR$. In practice, the electric-mode limit responses are most readily attainable with materials possessing plasmonic responses, like gold and silver, while for magnetic modes, high-index, low-loss materials like silicon, $\varepsilon_{\mathrm{Si}}\sim 14$, are required.

### B. Near- and far-field spectra

We saw above that the use of Eqs. (2), (4), and (6) allows rapid determination of the optimal far-field responses of small particles, but the resonant response is also of interest due to the near-field enhancements it induces. It has recently been pointed out, however, that there is a red shift of the optimal near-field enhancements with respect to the cross section-maxima [30–32].

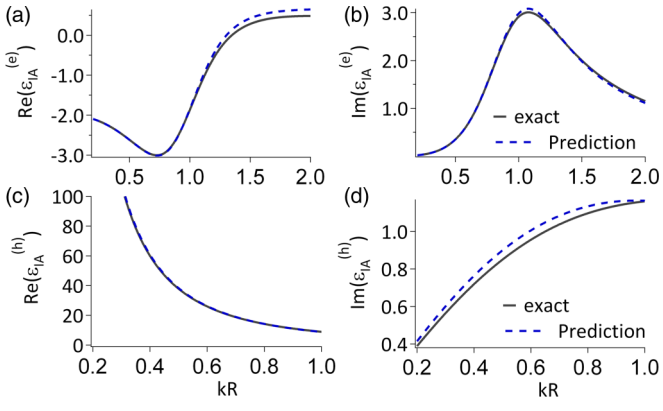


FIG. 4. Real (a, c) and imaginary (b, d) parts of the dielectric permittivity satisfying IA in the electric (a, b) and magnetic (c, d) dipole modes. Exact predictions (solid gray lines) and approximate predictions [dashed (blue) lines].

We derived approximate and *exact* formulas in Eqs. (10) and (C1), respectively, in order to quantify these near-field spectral shifts for both electric- and magnetic-field enhancements. Our approximate expression for the electric-field enhancement factor $\langle I_{\mathrm{enh}}^{(e)}\rangle$, given in Eq. (10a), is quite similar to a formula derived by Yuffa *et al.* [32], but those authors used somewhat different definitions of field enhancements (apparently due to the fact that they looked at scattered fields rather than the total fields considered here).

Angle-averaged local electric- and magnetic-field intensity enhancement factors, $\langle I_{\mathrm{enh}}^{(e)}\rangle$ and $\langle I_{\mathrm{enh}}^{(h)}\rangle$, are functions of the normalized distance to the particle center, $\eta\equiv kr$, and can be defined as

$$\begin{aligned}\left\langle I_{\mathrm{enh}}^{(e)}\right\rangle &\equiv \frac{\int d\Omega\|\mathbf{E}_{\mathrm{tot}}(\eta\hat{\mathbf{r}})\|^2}{4\pi\|\mathbf{E}_{\mathrm{exc}}(\mathbf{0})\|^2}\\ &\simeq 1+\sum_{n=1}^{\infty} g_n^{(1)}(\eta)|b_n|^2+g_n^{(2)}(\eta)|a_n|^2, \qquad (10a)\\ \left\langle I_{\mathrm{enh}}^{(h)}\right\rangle &\equiv \frac{\int d\Omega\|\mathbf{H}_{\mathrm{tot}}(\eta\hat{\mathbf{r}})\|^2}{4\pi\|\mathbf{H}_{\mathrm{exc}}(\mathbf{0})\|^2}\\ &\simeq 1+\sum_{n=1}^{\infty} g_n^{(1)}(\eta)|a_n|^2+g_n^{(2)}(\eta)|b_n|^2, \qquad (10b)\end{aligned}$$

where $\mathbf{E}_{\mathrm{tot}}$ and $\mathbf{H}_{\mathrm{tot}}$ are, respectively, the total electric and magnetic fields outside the particle. The functions $g_n^{(1)}(\eta)$ and $g_n^{(2)}(\eta)$ of Eq. (10) are given by

$$\begin{aligned}g_n^{(1)}(\eta) &\equiv \frac{2n+1}{2}\left|h_n^{(+)}(\eta)\right|^2,\\ g_n^{(2)}(\eta) &\equiv \frac{1}{2}\left[(n+1)\left|h_{n-1}^{(+)}(\eta)\right|^2+n\left|h_{n+1}^{(+)}(\eta)\right|^2\right].\end{aligned} \tag{11}$$

The approximation used in deriving Eqs. (10) is accurate only as long as the respective electric and magnetic excitation fields can be approximated by their values at the center of the particle, $\mathbf{E}_{\mathrm{exc}}(\mathbf{0})$ and $\mathbf{H}_{\mathrm{exc}}(\mathbf{0})$. Although this is generally quite accurate at small $kr$ values, its validity can be tested with the exact expressions for near-field enhancements given in Appendix C.

The electric-field enhancement formulas in Eq. (10) explain why the maximum of the near-field enhancements are generally red-shifted with respect to their cross-section maxima. The spherical Hankel functions are rapidly diverging functions in the $kr\to 0$ limit (due to the existence of evanescent waves near the current sources [30]), which shifts the near-field maximum to smaller values of $k$ compared to the values of $k$ which maximize the amplitude of a Mie coefficient.

In Figs. 5(a) and 5(c), we plot the scattering efficiencies, $Q_{\mathrm{scat}}=\sigma_{\mathrm{scat}}/\sigma_{\mathrm{geom}}$ ($\sigma_{\mathrm{geom}}=\pi R^2$ is the geometrical cross section), of $R=40$-nm-radius spheres whose permittivities are chosen so that electric (magnetic) dipole ULs are, respectively, reached when $kR=0.5$ ($\bar{\varepsilon}_{\mathrm{UL}}^{(e)}=-2.65$, $\bar{\varepsilon}_{\mathrm{UL}}^{(h)}=37.9$). Total efficiencies are plotted by dashed (blue) lines, while dipole electric and magnetic contributions are plotted by dotted (red)

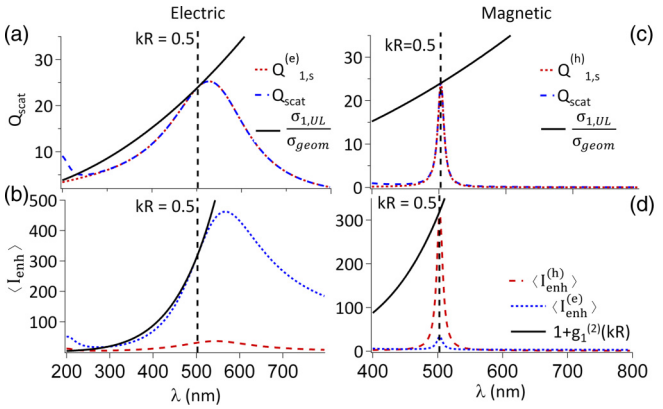


FIG. 5. Cross-section efficiencies (a, c) and field enhancements at the particle surface (b, d) for $R = 40$–nm spheres satisfying the dipole UL in the electric (a, b) and magnetic (c, d) modes at $kR = 0.5$. Maximal dipole contributions to $Q$ and $\langle I_{\text{enh}}^{(e,h)}\rangle$ are plotted as solid black lines.

lines. UL dipole efficiencies are plotted as solid black lines as a reference. Angle-averaged field enhancements $\langle I_{\text{enh}}^{(e,h)}\rangle$ for both electric and magnetic fields at the particle surface are plotted in Figs. 5(b) and 5(d). Maximal dipole contributions to $Q$ and $\langle I_{\text{enh}}^{(e,h)}\rangle$ for electric and magnetic modes, respectively, are plotted as solid black lines in Figs. 5. Their strongly decreasing behaviors as a function of an increasing size parameter explains why we focused attention on small particles (with respect to $\lambda$).

We remark that the cross sections in Fig. 5(a), being weighted by the wavelength squared as seen in Eq. (6), have their maximal cross sections red-shifted with respect to the UL frequency. The maximum field enhancements $\langle I_{\text{enh}}^{(e,h)}\rangle$ are, however, even more red-shifted than the cross sections according to the arguments presented following Eq. (11). Both red shifts are far less pronounced for narrower resonances like those of the magnetic dipole UL and IA in Figs. 5(c), 5(d), 6(c), and 6(d).

As in the UL case, the spectral behavior of IA spheres can be studied by plotting the evolution of the absorption efficiency, $Q_{\text{abs}} = \sigma_{\text{abs}}/\sigma_{\text{geom}}$, as shown in Figs. 6(a) and 6(c), for the dipole electric [Fig. 6(a)] and dipole magnetic [Fig. 6(b)] modes of $R = 40$–nm spheres designed to reach IA at a size parameter of $kR = 0.5$ ($\bar{\varepsilon}_{\text{IA}}^{(e)} = -2.62 + 0.35i$, $\bar{\varepsilon}_{\text{IA}}^{(h)} = 37.9 + i0.85$).

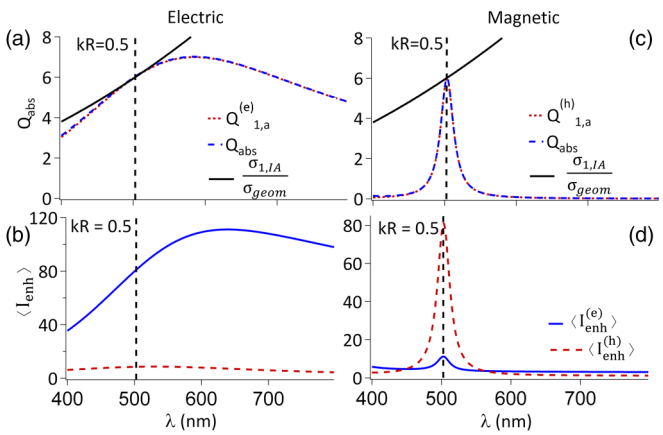


FIG. 6. The same plots as in Fig. 5 except that absorption efficiencies in dipole IA particles in (a) and (c) are plotted at $kR = 0.5$. Dipole absorption limit efficiencies are plotted by solid black lines.

## IV. ALGEBRAIC EXPRESSIONS FOR OPTIMAL MAGNETIC LIGHT-PARTICLE INTERACTIONS

The previous results have shown that the conditions to reach IA and the UL in the magnetic dipole mode are in fact very close to one another. From Figs. 3(b) and 4(c), one finds that the permittivity required to reach the UL at $kR = 0.5$ and the real part of the permittivity necessary to reach IA at that same size are both approximately $\varepsilon \approx 38$. We further illustrate this point by comparing the exact values of $\varepsilon_{\text{UL}}$ and $\text{Re}\{\varepsilon_{\text{IA}}\}$ over a range of $kR$ in Fig. 7(a).

An explanation of this property is found by examining the limits equations giving the UL and IA conditions (see Appendix A for additional details). From inspection of Eq. (A12), one sees that the condition for IA in the magnetic dipole mode is

$$S_1^{(h)} = 0 \iff \varphi_1(k_s R) = \varphi_1^{(-)}(kR), \tag{12}$$

where the $\varphi$ functions are defined in Eq. (A13). In the small-particle limit, $\lim_{x\to 0} h_n^{(-)}(x) = -i y_n(x)$, and the equation for IA becomes, for $kR \ll 1$,

$$S_1^{(h)} = 0 \iff \varphi_1(k_s R) \backsimeq \varphi_1^{(2)}(kR), \tag{13}$$

which is identical to the magnetic dipole UL [see Eqs. (7), (9), and (A12)],

$$\left(K_1^{(h)}\right)^{-1} = 0 \iff \varphi_1(k_s R) = \varphi_1^{(2)}(kR). \tag{14}$$

If the previous equations are solved in the $kR \to 0$ limit, the following simple expressions are found for the IA and UL conditions:

$$\varepsilon_{\text{UL}} \backsimeq \text{Re}(\varepsilon_{\text{IA}}) \backsimeq \frac{10}{(kR)^2} \backsimeq \left(\frac{\pi}{kR}\right)^2, \tag{15}$$

$$\text{Im}\{\varepsilon_{\text{IA}}\} \backsimeq \frac{49}{2}\left(1 - \sqrt{\frac{5}{6}}\right)kR - \frac{203}{24\sqrt{30}}(kR)^3. \tag{16}$$

This approximate expression is compared with exact calculations in Fig. 7(b).

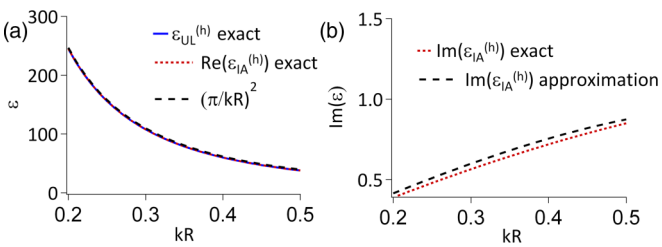


FIG. 7. Permittivities satisfying the magnetic dipole UL, $\varepsilon_{\text{UL}}^{(h)}$ [solid (blue) line], and satisfying the magnetic IA, $\varepsilon_{\text{IA}}^{(h)}$ [dotted (red) line], as functions of $kR$: real parts (a) and imaginary parts (b). Approximate algebraic expressions of Eqs. (15) and (16) are plotted by the dashed black line.

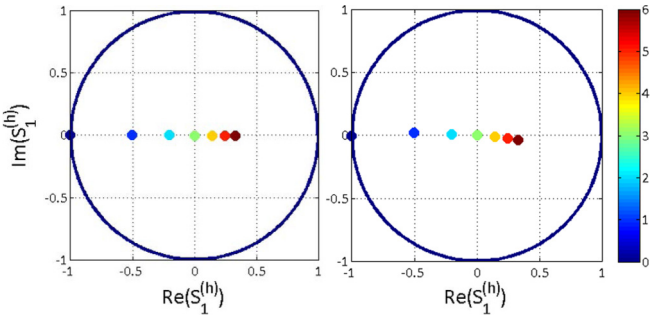


FIG. 8. Values of $S_1^{(h)}$ for permittivities calculated from Eq. (17) for $kR = 0.4$ and $kR = 0.8$; the color bar indicates the value of $j$ at each point.

## V. TRANSITION FROM THE UNITARY LIMIT TO IDEAL ABSORPTION

One sees in Fig. 7 that a magnetic dipole UL response can transform into an IA response with the appropriate amount of added absorption. This is illustrated in Fig. 8, which plots the values of the complex $S_1^{(h)}$ coefficient as the permittivity ranges from the UL permittivity, $\varepsilon_{\rm UL}^{(h)}$, to and beyond the IA permittivity, $\varepsilon_{\rm IA}^{(h)}$, according to the following functions for spheres with $kR = 0.4$ and $kR = 0.8$:

$$\begin{aligned} \varepsilon &= \varepsilon_{\rm UL}^{(h)} + j\frac{\left(\varepsilon_{\rm UL}^{(h)} - \varepsilon_{\rm IA}^{(h)}\right)}{3}, \\ kR &= 0.4 \quad kR = 0.8 \\ \varepsilon_{\rm UL}^{(h)} &= 59.94 \quad \varepsilon_{\rm UL}^{(h)} = 14.3 \\ \varepsilon_{\rm IA}^{(h)} &= 59.93 + i0.72 \quad \varepsilon_{\rm IA}^{(h)} = 14.2 + i1.1 \end{aligned} \tag{17}$$

where $j$ is an integer between 0 and 6 in each case. The UL value of $S_1^{(h)} = -1$ corresponds to $j = 0$, while the $S_1^{(h)} = 0$ IA limit occurs at $j = 3$.

The permittivities, scattering efficiencies, and field enhancements at the surface of the particles for the values of Eq. (17) and Fig. 8 are listed in Tables I and II. A comparison of Tables I and II shows that although the larger $kR = 0.8$ spheres require considerably smaller permittivities, this comes at the expense of much weaker field enhancements.

TABLE I. Cross section and magnetic- and electric-field enhancement factors for $kR = 0.4$–sized particles.

| $j$ | $\varepsilon$ | $Q_{1,\rm ext}^{(h)}$ | $Q_{1,\rm scat}^{(h)}$ | $Q_{1,\rm abs}^{(h)}$ | $\langle I_{\rm enh}^{(h)}\rangle$ | $\langle I_{\rm enh}^{(e)}\rangle$ |
|---|---|---|---|---|---|---|
| 0 | 59.94 | 37.5 | 37.5 | 0 | 1168 | 71 |
| 1 | $59.94 + 0.24i$ | 28.1 | 21.1 | 7 | 657 | 42 |
| 2 | $59.94 + 0.48i$ | 22.5 | 13.5 | 9 | 421 | 28 |
| 3 | $59.94 + 0.72i$ | 18.8 | 9.4 | 9.4 | 293 | 20 |
| 4 | $59.94 + 0.96i$ | 16.1 | 6.9 | 9.2 | 215 | 16 |
| 5 | $59.94 + 1.2i$ | 14.1 | 5.3 | 8.8 | 165 | 13 |
| 6 | $59.94 + 1.44i$ | 12.5 | 4.2 | 8.3 | 131 | 11 |

TABLE II. Cross section and magnetic- and electric-field enhancement factors for $kR = 0.8$–sized particles.

| $j$ | $\varepsilon$ | $Q_{1,\rm ext}^{(h)}$ | $Q_{1,\rm scat}^{(h)}$ | $Q_{1,\rm abs}^{(h)}$ | $\langle I_{\rm enh}^{(h)}\rangle$ | $\langle I_{\rm enh}^{(e)}\rangle$ |
|---|---|---|---|---|---|---|
| 0 | 14.3 | 9.4 | 9.4 | 0 | 25 | 10 |
| 1 | $14.2 + 0.37i$ | 7 | 5.3 | 1.8 | 14.9 | 7.7 |
| 2 | $14.2 + 0.73i$ | 5.6 | 3.4 | 2.3 | 10.2 | 6.4 |
| 3 | $14.2 + 1.1i$ | 4.7 | 2.3 | 2.4 | 7.6 | 5.7 |
| 4 | $14.2 + 1.5i$ | 4 | 1.7 | 2.3 | 6.1 | 5.3 |
| 5 | $14.1 + 1.8i$ | 3.5 | 1.3 | 2.2 | 5.1 | 5 |
| 6 | $14.1 + 2.2i$ | 3.2 | 1.1 | 2.1 | 4.4 | 4.8 |

## VI. CONCLUSION

In this work, we have derived accurate approximate expressions of the particle polarizability and used these to study ULs and IA limits of the dipolar modes of small particles. We have also derived formulas that allow a qualitative and quantitative analysis of the displacement of the near-field maxima with respect to far-field maxima. We have applied this approach to both metallic and dielectric nanoparticles and placed emphasis on magnetic dipolar resonances in high-index dielectric particles. In the latter case, we derived closed expressions for the UL and IA in the small-particle limit.

Although this work focused on the study of particles that are small with respect to $\lambda$, on account of their ability to produce large field enhancements, the full formulas given in the appendixes are valid for spheres of arbitrary size and should prove useful in analyzing finite-size corrections of larger resonant particles (as illustrated by the detailed analysis of the $kR = 0.8$ simulations in Sec. V). This study should help in the design of highly efficient photonic resonators, which are of crucial importance to strengthen the light-matter interaction at subwavelength scales.

## ACKNOWLEDGMENTS

This work was carried out thanks to the support of the A*MIDEX project (No. ANR-11-IDEX-0001-02) funded by the French Government program Investissements d'Avenir, managed by the French National Research Agency (ANR), and within the context of the France-Australian International Associated Laboratory, ALPhFA: Associated Laboratory for Photonics. The authors would like to thank Jean-Paul Hugonin and Boris Kuhlmey for fruitful discussions.

## APPENDIX A: MULTIPOLE SCATTERING THEORY

Notations in the literature vary considerably, and we begin this section by reviewing our notation for vector partial-wave (VPW) expansions. Let us consider an arbitrary-shaped scatterer characterized by permittivity $\varepsilon_s$ and permeability $\mu_s$ placed in a background medium of permittivity $\varepsilon_b$, and permeability $\mu_b$.

The Foldy-Lax excitation field of a particle can be developed on the basis of regular (source-free) VPWs of the first type, traditionally denoted $\mathbf{M}_{n,m}^{(1)}$ (magnetic modes) and $\mathbf{N}_{n,m}^{(1)}$ (electric modes) ($n$ and $m$ are, respectively, the total and

projected angular momentum of the VPW, i.e.,

$$\mathbf{E}_{\rm exc}(\mathbf{r}) = \sum_{n,m} \left\{ \mathbf{M}^{(1)}_{n,m}(k\mathbf{r}) e^{(h)}_{n,m} + \mathbf{N}^{(1)}_{n,m}(k\mathbf{r}) e^{(e)}_{n,m} \right\}$$
$$\equiv [\mathbf{M}^{(1)}(k\mathbf{r}), \mathbf{N}^{(1)}(k\mathbf{r})] \begin{pmatrix} e^{(h)} \\ e^{(e)} \end{pmatrix}, \tag{A1}$$

where the $(e)$ and $(h)$ superscripts indicate electric- and magnetic-type VPWs, respectively. In the second line of Eq. (A1), we have suppressed the summations by adopting a more compact matrix notation where expansion coefficients of the excitation field are placed in an infinite-column matrix, and the corresponding VPW functions, $\mathbf{M}^{(1)}_{n,m}(k\mathbf{r})$ and $\mathbf{N}^{(1)}_{n,m}(k\mathbf{r})$, as elements of an infinite-row "matrix" [33].

The field scattered by the particle must satisfy outgoing boundary conditions which can be obtained by superpositions of the VPWs with VPWs including a second type of partial wave, $\mathbf{M}^{(2)}_{n,m}$ and $\mathbf{N}^{(2)}_{n,m}$, which are obtained by replacing the spherical Bessel functions, $j_n(x)$, in VPWs of the first type with spherical Neumann functions, $y_n(x)$. It proves useful in the following to describe waves satisfying incoming boundary conditions. Incoming $(-)$ and outgoing $(+)$ VPWs can be expressed as

$$\mathbf{M}^{(\pm)}_{n,m}(k\mathbf{r}) \equiv \tfrac{1}{2}\left(\mathbf{M}^{(1)}_{n,m}(k\mathbf{r}) \pm i\mathbf{M}^{(2)}_{n,m}(k\mathbf{r})\right), \tag{A2}$$

and likewise for $\mathbf{N}^{(\pm)}_{n,m}$. The scattered field can then be developed in terms of VPWs with outgoing boundary conditions, again using the matrix notation,

$$\mathbf{E}_{\rm scat}(\mathbf{r}) = [\mathbf{M}^{(+)}_{n,m}(k\mathbf{r}), \mathbf{N}^{(+)}_{n,m}(k\mathbf{r})] \begin{pmatrix} f^{(h)}_{n,m} \\ f^{(e)}_{n,m} \end{pmatrix}. \tag{A3}$$

In the multipole formulation, the $T$ matrix, by definition, expresses the linear relationship between the coefficients of the excitation field $\mathbf{E}_{\rm exc}$ and the multipolar coefficients of the scattered field:

$$\begin{pmatrix} f^{(h)} \\ f^{(e)} \end{pmatrix} \equiv T \begin{pmatrix} e^{(h)} \\ e^{(e)} \end{pmatrix}. \tag{A4}$$

It is important to keep in mind in what follows that the fields $\mathbf{E}_{\rm exc}$ and $\mathbf{E}_{\rm scat}$ are abstractions, and the only field which is physically present is the *total* field, $\mathbf{E}_{\rm tot} = \mathbf{E}_{\rm exc} + \mathbf{E}_{\rm scat}$.

The $S$-matrix approach adopts an alternative decomposition of the total fields in terms of $\mathbf{E}_{\rm in}$ and $\mathbf{E}_{\rm out}$, which, respectively, satisfy incoming and outgoing boundary conditions, i.e., $\mathbf{E}_{\rm tot} = \mathbf{E}_{\rm in} + \mathbf{E}_{\rm out}$, with

$$\mathbf{E}_{\rm in}(\mathbf{r}) = [\mathbf{M}^{(-)}_{n,m}(k\mathbf{r}), \mathbf{N}^{(-)}_{n,m}(k\mathbf{r})] \begin{pmatrix} a^{(h,-)}_{n,m} \\ a^{(e,-)}_{n,m} \end{pmatrix},$$
$$\mathbf{E}_{\rm out}(\mathbf{r}) = [\mathbf{M}^{(+)}_{n,m}(k\mathbf{r}), \mathbf{N}^{(+)}_{n,m}(k\mathbf{r})] \begin{pmatrix} a^{(h,+)}_{n,m} \\ a^{(e,+)}_{n,m} \end{pmatrix}. \tag{A5}$$

The matrix $S$ then relates the incoming field coefficients, $a^{(h,-)}_{n,m}$, to the outgoing field coefficients, $a^{(h,-)}_{n,m}$:

$$\begin{pmatrix} a^{(h,+)}_{n,m} \\ a^{(e,+)}_{n,m} \end{pmatrix} \equiv S \begin{pmatrix} a^{(h,-)}_{n,m} \\ a^{(e,-)}_{n,m} \end{pmatrix}. \tag{A6}$$

The relationship between the $S$ and the $T$ matrices can be obtained algebraically by invoking the definitions of Eq. (A2) and the fact that both matrices describe the same total electric field $\mathbf{E}_{\rm tot}$ to find

$$S = I + 2T, \tag{A7}$$

where $I$ is the identity matrix. Flux conservation for a lossless scatterer requires the unitarity of the $S$-matrix, which leads directly to the energy conservation condition of the $T$ matrix,

$$T + T^\dagger = -2T^\dagger T, \tag{A8}$$

which has also been called the Ward identity or "optical theorem."

Finally, the reaction matrix, $K$, relates the total field outside the scatterer as a superposition of regular fields, $\mathbf{E}_{\rm reg}$, developed in terms of VPWs of the first type, and singular fields, $\mathbf{E}_{\rm sing}$, developed in terms of the second, i.e., Neumann, type:

$$\mathbf{E}_{\rm reg}(\mathbf{r}) = \left[\mathbf{M}^{(1)}_{n,m}(k\mathbf{r}), \mathbf{N}^{(1)}_{n,m}(k\mathbf{r})\right] \begin{pmatrix} r^{(h)}_{n,m} \\ r^{(e)}_{n,m} \end{pmatrix},$$
$$\mathbf{E}_{\rm sing}(\mathbf{r}) = \left[\mathbf{M}^{(2)}_{n,m}(k\mathbf{r}), \mathbf{N}^{(2)}_{n,m}(k\mathbf{r})\right] \begin{pmatrix} d^{(h)}_{n,m} \\ d^{(e)}_{n,m} \end{pmatrix}. \tag{A9}$$

The $K$ matrix relates the coefficients of these two field descriptions:

$$\begin{pmatrix} d^{(h)}_{n,m} \\ d^{(e)}_{n,m} \end{pmatrix} \equiv K \begin{pmatrix} r^{(h)}_{n,m} \\ r^{(e)}_{n,m} \end{pmatrix}. \tag{A10}$$

For the $K$ matrix, the lossless condition is that $K$ is Hermitian, $K = K^\dagger$. The relations between the $K$ and the $S$ and $T$ matrices can again be obtained from the definitions of Eqs. (A4), (A6), and (A10) and by taking into account the different VPW types. After some algebraic manipulations, one obtains the relations

$$K = i(S - I)(I + S)^{-1} \Leftrightarrow S = (I - iK)(I + iK)^{-1}. \tag{A11}$$

The relations between the $K$ and the $S$ matrices in Eq. (A11) are known as a Cayley transformation, while the relations between $T$ and $K$ matrices are given in Eq. (1). We remark that for spherically symmetric scatterers, these matrices are all diagonal and their elements have simple expressions in terms of the scattering phase shifts of the partial waves, $\delta_n$, as discussed, for example, by van de Hulst [8, chap. 10] and Newton [34]. These are $S_n = e^{2i\delta_n}$, $T_n = i \sin\delta_n e^{i\delta_n}$, and $K_n = -\tan\delta_n$, and they automatically satisfy all the formal relations among the $S$, $T$, and $K$ matrices discussed in this work (and the energy conservation relations, provided that $\delta_n$ is real valued).

For spherical particles, one has analytic expressions for all the $S$, $T$, and $K$ in the context of Mie theory, where their elements are diagonal in the multipole basis and depend only on the total angular momentum number, $n$,

$$T^{(e)}_n = -\frac{j_n(kR)}{h^{(+)}_n(kR)} \frac{\overline{\varepsilon}_s \varphi_n(kR) - \varphi_n(k_s R)}{\overline{\varepsilon}_s \varphi^{(+)}_n(kR) - \varphi_n(k_s R)},$$
$$S^{(e)}_n = -\frac{h^{(-)}_n(kR)}{h^{(+)}_n(kR)} \frac{\overline{\varepsilon}_s \varphi^{(-)}_n(kR) - \varphi_n(k_s R)}{\overline{\varepsilon}_s \varphi^{(+)}_n(kR) - \varphi_n(k_s R)}, \tag{A12}$$
$$K^{(e)}_n = -\frac{j_n(kR)}{y_n(kR)} \frac{\overline{\varepsilon}_s \varphi_n(kR) - \varphi_n(k_s R)}{\overline{\varepsilon}_s \varphi^{(2)}_n(kR) - \varphi_n(k_s R)},$$

where $\overline{\varepsilon}_s \equiv \frac{\varepsilon_s}{\varepsilon_b}$. The formulas for magnetic-mode response functions, $S_n^{(h)}$, $T_n^{(h)}$, and $K_n^{(h)}$, are obtained simply by replacing $\overline{\varepsilon}_s$ in the above formulas with the magnetic permeability contrast $\overline{\mu}_s = \frac{\mu_s}{\mu_b}$.

The functions, $\varphi_n$, $\varphi_n^{(2)}$, and $\varphi_n^{(\pm)}$, in Eqs. (A12) are modified logarithmic derivatives of the Ricatti spherical Bessel functions and are defined as

$$\begin{aligned} \varphi_n(z) &\equiv \varphi_n^{(1)}(z) \equiv \frac{[z j_n(z)]'}{j_n(z)}, \\ \varphi_n^{(2)}(z) &\equiv \frac{[z y_n(z)]'}{y_n(z)}, \quad \varphi_n^{(\pm)}(z) \equiv \frac{[z h_n^{(\pm)}(z)]'}{h_n^{(\pm)}(z)}, \end{aligned} \tag{A13}$$

with $j_n$ and $y_n$, respectively, denoting $n$th-order spherical Bessel and Neumann functions, and $h_n^{(\pm)} = j_n \pm i y_n$ the incoming $(-)$ and outgoing $(+)$ spherical Hankel functions.

## APPENDIX B: EXPANSIONS FOR ARBITRARY MULTIPOLE ORDER

We give below the development up to sixth order in $kR$ of the inverse reaction matrix for $\overline{\mu}_s = 1$. In most of the predictions and simulations in this work, fourth-order expansion in $kR$ suffices, but the sixth order sometimes proved useful to test convergence or to achieve additional accuracy:

$$\left[K_n^{(e)}\right]^{-1} \simeq -\frac{(2n-1)!!(2n+1)!!}{(n+1)(\overline{\varepsilon}_s - 1)x^{2n+1}}\left((n\overline{\varepsilon}_s + n + 1) + \frac{(2n+1)((n-2)\overline{\varepsilon}_s + n + 1)}{(2n-1)(2n+3)}x^2 + x^4 C_4^{(e)} + x^6 C_6^{(e)}\right), \tag{B1a}$$

$$\left[K_n^{(h)}\right]^{-1} \simeq -\frac{(2n+1)(2n+3)(2n-1)!!(2n+1)!!}{(\overline{\varepsilon}_s - 1)x^{2n+3}}\left(1 + \frac{(2n - 2\overline{\varepsilon}_s + 3)}{(2n+1)(2n+5)}x^2 + x^4 C_4^{(h)} + x^6 C_6^{(h)}\right), \tag{B1b}$$

where the fourth- and sixth-order coefficients, respectively, $C_4$ and $C_6$, are given by

$$C_4^{(e)} = (2n+1)\frac{(n+3)(n+1)^2 + (n-4)(n+3)(n+1)\overline{\varepsilon}_s - (2n-3)\overline{\varepsilon}_s^2}{(n+1)(2n-3)(2n+3)^2(2n+5)}, \tag{B2a}$$

$$C_4^{(h)} = \frac{(n+4)(2n+3)^2 - 4(n+4)(2n+3)\overline{\varepsilon}_s - (2n-1)\overline{\varepsilon}_s^2}{(2n-1)(2n+3)(2n+5)^2(2n+7)}, \tag{B2b}$$

$$C_6^{(e)} = (2n+1)\frac{(n+1)\left(2n^2+15n+30\right)[(n+1) + (n-6)\overline{\varepsilon}_s] - 3(2n-5)\overline{\varepsilon}_s^2[(2n+9) + 2\overline{\varepsilon}_s]}{3(n+1)(2n-5)(2n+3)^3(2n+5)(2n+7)}, \tag{B2c}$$

$$C_6^{(h)} = \frac{(2n+3)(2n^2+19n+47)[(2n+3) - 6\overline{\varepsilon}_s] - 3(2n-3)\overline{\varepsilon}^2[(2n+11) + 2\overline{\varepsilon}]}{3(2n-3)(2n+3)(2n+5)^3(2n+7)(2n+9)}, \tag{B2d}$$

and the double factorial operator !! is defined such that

$$n!! = \prod_{k=0}^{m}(n-2k) = n(n-2)(n-4)\ldots, \tag{B3}$$

where $m = \mathrm{Int}[(n+1)/2] - 1$ with $0!! = 1$, or in terms of ordinary factorials via the relations $(2n-1)!! = \frac{(2n)!}{2^n n!}$ and $(2n)!! = 2^n n!$ for $n = 0,1,2,\ldots$.

## APPENDIX C: EXACT FORMULAS FOR NEAR-FIELD ENHANCEMENTS

Formally exact expressions for the field enhancement factors, Eq. (10) can be written

$$\begin{aligned} \left\langle I_{\mathrm{enh}}^{(e)}\right\rangle &= \sum_{n=1}^{\infty}\left\{\widetilde{g}_n^{(1,e)}(\eta)\left|T_n^{(h)}\right|^2 + \widetilde{g}_n^{(2,e)}(\eta)\left|T_n^{(e)}\right|^2\right\}, \\ \left\langle I_{\mathrm{enh}}^{(h)}\right\rangle &= \sum_{n=1}^{\infty}\left\{\widetilde{g}_n^{(1,h)}(kr)\left|T_n^{(e)}\right|^2 + \widetilde{g}_n^{(2,h)}(kr)\left|T_n^{(h)}\right|^2\right\}. \end{aligned} \tag{C1}$$

We remark that Eq. (C1) is valid numerically only if the infinite multipole summation is cut off to a value $n_{\max} > kr$, with $r$ being the distance from the center of the particle. This differs from the approximate formula of Eq. (10), where the multipole summation can be stopped at the usual Mie cutoff condition of $n_{\max} > kR$.

The enhancement functions of Eq. (C1) are written

$$\begin{aligned} \widetilde{g}_n^{(1,e)}(\eta) &= \frac{2n+1}{2}\left|\frac{j_n(\eta)}{T_n^{(h)}} + h_n^{(+)}(\eta)\right|^2, \\ \widetilde{g}_n^{(2,e)}(\eta) &= \frac{n+1}{2}\left|\frac{j_{n-1}(\eta)}{T_n^{(e)}} + h_{n-1}^{(+)}(\eta)\right|^2 \\ &\quad + \frac{n}{2}\left|\frac{j_{n+1}(\eta)}{T_n^{(e)}} + h_{n+1}^{(+)}(\eta)\right|^2, \\ \widetilde{g}_n^{(1,h)}(\eta) &= \frac{2n+1}{2}\left|\frac{j_n(\eta)}{T_n^{(e)}} + h_n^{(+)}(\eta),\right|^2 \\ \widetilde{g}_n^{(2,h)}(\eta) &= \frac{n+1}{2}\left|\frac{j_{n-1}(\eta)}{T_n^{(h)}} + h_{n-1}^{(+)}(\eta)\right|^2 \\ &\quad + \frac{n}{2}\left|\frac{j_{n+1}(\eta)}{T_n^{(h)}} + h_{n+1}^{(+)}(\eta)\right|^2. \end{aligned} \tag{C2}$$

[1] L. Novotny and B. Hecht, *Principles of Nano-Optics* (Cambridge University Press, Cambridge, UK, 2006).
[2] V. Grigoriev, A. Tahri, S. Varault, B. Rolly, B. Stout, J. Wenger, and N. Bonod, Phys. Rev. A **88**, 011803 (2013).
[3] S. Enoch and N. Bonod, *Plasmonics: From Basics to Advanced Topics* (Springer, Berlin, 2012).
[4] M. Agio and A. Alù, *Optical Antennas* (Cambridge University Press, Cambridge, UK, 2013).
[5] H. A. Atwater and A. Polman, Nat. Mater. **9**, 205 (2010).
[6] L. Novotny and N. van Hulst, Nature Photon. **5**, 83 (2011).
[7] G. Baffou and R. Quidant, Laser Photon. Rev. **7**, 171 (2013).
[8] H. C. van de Hulst, *Light Scattering by Small Particles*. *Structure of Matter Series* (Dover, Mineola, NY, 1981).
[9] C. F. Bohren and D. R. Huffman, *Absorption and Scattering of Light by Small Particles* (Wiley Science, New York, 1983).
[10] M. Mishchenko, L. Travis, and A. Lacis, *Scattering, Absorption, and Emission of Light by Small Particles* (Cambridge University Press, Cambridge, UK, 2002), p. 462.
[11] N. G. Khlebtsov, J. Quant. Spectrosc. Radiat. Transfer **123**, 184 (2013).
[12] V. Grigoriev, N. Bonod, J. Wenger, and B. Stout, ACS Photon. **2**, 263 (2015).
[13] E. C. Le Ru, W. R. C. Somerville, and B. Auguié, Phys. Rev. A **87**, 012504 (2013).
[14] B. Rolly, B. Bebey, S. Bidault, B. Stout, and N. Bonod, Phys. Rev. B **85**, 245432 (2012).
[15] M. K. Schmidt, R. Esteban, J. J. Sáenz, I. Suárez-Lacalle, S. Mackowski, and J. Aizpurua, Opt. Express **20**, 13636 (2012).
[16] M. R. Shcherbakov, D. N. Neshev, B. Hopkins, A. S. Shorokhov, I. Staude, E. V. Melik-Gaykazyan, M. Decker, A. A. Ezhov, A. E. Miroshnichenko, I. Brener *et al.*, Nano Lett. **14**, 6488 (2014).
[17] G. Boudarham, R. Abdeddaim, and N. Bonod, Appl. Phys. Lett. **104**, 021117 (2014).
[18] R. M. Bakker, D. Permyakov, Y. F. Yu, D. Markovich, R. Paniagua-Domínguez, L. Gonzaga, A. Samusev, Y. Kivshar, B. Lukyanchuk, and A. I. Kuznetsov, Nano Lett. **15**, 2137 (2015).
[19] X. Zambrana-Puyalto and N. Bonod, Phys. Rev. B **91**, 195422 (2015).
[20] S. Makarov, S. I. Kudryashov, I. Mukhin, A. Mozharov, V. Milichko, A. Krasnok, and P. A. Belov, Nano Lett. **15**, 6187 (2015).
[21] G. C. Des Francs, C. Girard, A. Bruyant, and A. Dereux, J. Microsc. (NFO9) **229**, 302 (2008).
[22] A. Moroz, J. Opt. Soc. Am. B **26**, 517 (2009).
[23] G. C. des Francs, A. Bouhelier, E. Finot, J. C. Weeber, A. Dereux, C. Girard, and E. Dujardin, Opt. Express **16**, 17654 (2008).
[24] S. Albaladejo, R. Gómez-Medina, L. S. Froufe-Pérez, H. Marinchio, R. Carminati, J. F. Torrado, G. Armelles, A. García-Martín, and J. J. Sáenz, Opt. Express **18**, 3556 (2010).
[25] B. Stout, A. Devilez, B. Rolly, and N. Bonod, J. Opt. Soc. Am. B **28**, 1213 (2011).
[26] D. Schebarchov, B. Auguie, and E. C. Le Ru, Phys. Chem. Chem. Phys. **15**, 4233 (2013).
[27] P. B. Johnson and R. W. Christy, Phys. Rev. B **6**, 4370 (1972).
[28] R. Fleury, J. Soric, and A. Alù, Phys. Rev. B **89**, 045122 (2014).
[29] S. Tretyakov, Plasmonics **9**, 935 (2014).
[30] F. Moreno, P. Albella, and M. Nieto-Vesperinas, Langmuir **29**, 6715 (2013).
[31] C. Menzel, E. Hebestreit, S. Mühlig, C. Rockstuhl, S. Burger, F. Lederer, and T. Pertsch, Opt. Express **22**, 9971 (2014).
[32] A. J. Yuffa, Y. Gutierrez, J. M. Sanz, R. A. de la Osa, J. M. Saiz, F. González, F. Moreno, and G. Videen, J. Opt. Soc. Am. A **32**, 1638 (2015).
[33] L. Tsang, J. Kong, K. Ding, and C. Ao, *Scattering of Electromagnetic Waves, Numerical Simulations* (John Wiley & Sons, New York, 2001), p. 736.
[34] R. G. Newton, *Scattering Theory of Waves and Particles*. *Texts and Monographs in Physics* (Springer, Berlin, 1982).